Dynamical simulations of radiation damage in magnesium aluminate spinel, $MgAl_2O_4$

2005 J. Phys.: Condens. Matter 17 875

(http://iopscience.iop.org/0953-8984/17/6/008)

INSTITUTE OF PHYSICS PUBLISHING JOURNAL OF PHYSICS: CONDENSED MATTER

J. Phys.: Condens. Matter **17** (2005) 875–891 doi:10.1088/0953-8984/17/6/008

Dynamical simulations of radiation damage in magnesium aluminate spinel, $MgAl_2O_4$

R Smith[1], D Bacorisen[1], B P Uberuaga[2], K E Sickafus[2], J A Ball[3] and R W Grimes[3]

[1] Department of Mathematical Sciences, Loughborough University, LE11 3TU, UK
[2] Los Alamos National Laboratory, Los Alamos, NM 87545, USA
[3] Department of Materials, Prince Consort Road, Imperial College, London SW7 2BP, UK

Received 13 October 2004, in final form 5 January 2005
Published 28 January 2005
Online at stacks.iop.org/JPhysCM/17/875

Abstract

Collision cascades in $MgAl_2O_4$ are investigated using molecular dynamics simulations in order to determine the threshold displacement energies, E_d, and the damage imparted to the lattice at energies of up to 5 keV. The value of E_d is determined for $MgAl_2O_4$ on each of the Mg, Al and O sublattices for different orientations of the primary knock-on atom (PKA). The lowest E_d required to create permanent defects was for an O PKA along the ⟨100⟩ direction with a value of 27.5 eV, while the highest was 277.5 eV along ⟨131⟩ for an Mg PKA. Higher energy cascades show that a much wider variety of defects remain after the collisional phase than for similar cascades in MgO but the number of Frenkel pairs produced is smaller. The predominant defects that form are antisite defects on the cation sublattice only and O and Mg split interstitials orientated along the ⟨110⟩ direction. Some Mg–Al split interstitials centred on an Mg site were also observed. However, some more extended defect complexes can also arise which have no well defined structure.

(Some figures in this article are in colour only in the electronic version)

1. Introduction

The mechanisms underlying irradiation of crystalline compounds by energetic particles have been the subject of extensive study. This quest can be explained partly by the need to derive new materials with enhanced radiation resistance. Accordingly, complex compounds such as zircon [1] ($ZrSiO_4$), pyrochlores [2] (materials with the structural formula $A_2B_2O_7$, where A and B are cations) and other oxides including magnesium aluminate [3] are currently being studied in order to understand the evolution of their defect structures after irradiation. It has been observed that exposure to radiation can cause adverse effects such as swelling or radiation-induced amorphization within certain crystal structures [4].

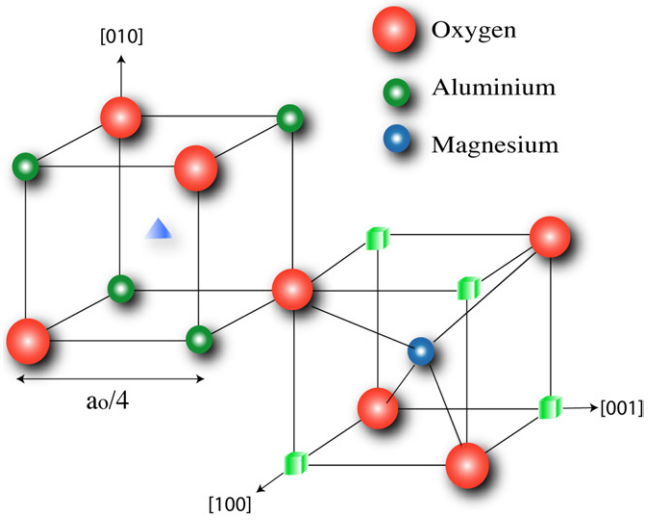

Figure 1. Structure of spinel. Mg ions sit at tetrahedral sites while Al ions occupy octahedral sites. The unoccupied tetrahedral sites are represented by (blue) triangles and octahedral sites are shown by the (green) cubes.

A good indication of the resistance to radiation damage of any material can be obtained from its threshold displacement energy, E_d. Here E_d is defined as the least amount of kinetic energy imparted to a lattice atom, usually referred to as the primary knock-on atom (PKA), which is necessary to displace permanently an atom (or ion in our case) from its original lattice site. This might include the creation of point defects in the lattice but it also could represent the situation where two lattice ions exchange sites but no other defects remain. In this work, E_d is derived for spinel, $MgAl_2O_4$, using molecular dynamics (MD) simulations. MD simulations offer an efficient way to understand the different mechanisms, such as point defect formation and annihilation, occurring within the irradiated crystal structure, which are difficult to monitor in real experiments due to their short lifetime. We also investigate the most common types of defect that form during a low energy radiation event, not only for PKA energies near the threshold but also over a wider energy range, namely 400 eV, 2 and 5 keV.

Spinel has a complex structure, as shown in figure 1. It has a face-centred cubic (fcc) structure with a unit cell consisting of eight $MgAl_2O_4$ formula units. Within this unit cell there are 32 octahedral interstices, 16 of which are occupied by trivalent aluminium ions. The divalent magnesium ions, also shown in figure 1, are located at eight of the 64 tetrahedral interstices. The remaining interstices are unoccupied but have the capability to accommodate cation species within a stable structure even at high temperature and pressure [5]. The cations are bonded to oxygen ions, which in this complex structure are dilated away from their ideal lattice positions. The physical and structural properties of magnesium aluminate spinel vary according to the following factors: the lattice parameter (a_0), the anion parameter (u, which is a measure of the oxygen dilation) and the cation inversion parameter (i, which is a measure of the antisite defects on the cation sub-lattice). These are detailed by Sickafus *et al* [6].

2. Model and numerical procedures

The potential used in this work is pairwise additive and consists of two parts: an electrostatic part and a standard Buckingham term [7]. For these cascade simulations, where, because

of the energetic collisions, the distances between ions can become very small, this potential was modified by splining it to a screened Coulomb potential for small particle separation [8], smoothly joined to the outer potential so that continuous first and second derivatives were preserved. A cut-off of the Buckingham potential term at a certain interatomic distance, r_2, was also implemented. Thus calculation of the overly attractive forces for small separation and the non-electrostatic part for large separation can be avoided. The potential gives a lattice parameter a_0 for $MgAl_2O_4$ of $a_0 = 8.122$ Å and a u value of $u = 0.395$. These are slightly higher than the quoted literature values; for example, [6] gives a value of $a_0 = 8.090$ Å and $u = 0.388$. Natural spinel also contains a number of antisite defects where the Mg and Al ions exchange places. Extensive experimental work [5, 11, 12] has been performed to investigate the distribution of these ions at octahedral and tetrahedral sites subject to different conditions. However, rather than running a series of simulations for different initial defect distributions, all our calculations were performed on perfectly ordered spinel. Future work may address the impact of cation disorder on the damage produced during irradiation.

The potential energy function for cation–cation interactions is thus given by

$$\phi(r) = \begin{cases} \text{ZBL} & r < r_0; \\ g(r) & r_0 \leqslant r < r_2; \\ V(r) & r \geqslant r_2. \end{cases}$$

The cation–anion interactions are modelled using a combination of the ZBL, Born–Mayer and Coulombic potentials, smoothly joined, with continuous first and second derivatives, by the splining function $g(r)$ as shown:

$$\phi(r) = \begin{cases} \text{ZBL} & r < r_0; \\ g(r) & r_0 \leqslant r < r_1; \\ A\exp\left(-\dfrac{r}{\rho}\right) + V(r) & r_1 \leqslant r < r_2; \\ V(r) & r \geqslant r_2. \end{cases}$$

The anion–anion interactions are described by adding a van der Waals term as follows:

$$\phi(r) = \begin{cases} \text{ZBL} & r < r_0; \\ g(r) & r_0 \leqslant r < r_1; \\ A\exp\left(-\dfrac{r}{\rho}\right) - \dfrac{C}{r^6} + V(r) & r_1 \leqslant r < r_2; \\ V(r) & r \geqslant r_2, \end{cases}$$

where the splining function is given by

$$g(r) = \mathrm{e}^{(f_1 + f_2 r + f_3 r^2 + f_4 r^3 + f_5 r^4 + f_6 r^5)}.$$

In the above equations r is the pair separation, $V(r)$ is the Coulomb potential and r_2 has a numerical value of 7.7 Å. The parameters for the spline are summarized in table 1 and the values for the constants A, ρ and C are shown in table 2. These potential parameters were chosen by fitting to experimental perfect lattice data of MgO and Al_2O_3 in addition to $MgAl_2O_4$.

In the MD simulations reported here we use a rigid-ion approximation in which each atom has its full formal charge. The Coulombic sums were evaluated using the fast multipole method [9]. Previous work on radiation damage of ionic systems has generally used Ewald sums [10]. However Ewald sums generally scale as $N^{3/2}$ where N is the number of particles in the system whereas the multipole method is O(N).The simulations were carried out by first choosing a specific PKA at the centre of the lattice to which excess kinetic energy is imparted along a specific crystallographic direction. The threshold energies were determined

Table 1. The parameters for the spline to the ZBL interaction.

	f_1	f_2	f_3	f_4	f_5	f_6
Mg–Mg	14.4507	−47.7977	122.4210	−175.9999	125.1304	−34.1480
Mg–Al	10.6531	−17.0984	27.9501	−36.8467	28.3526	−8.5504
Mg–O	11.0765	−31.3878	118.9207	−302.6137	367.5647	−167.4741
Al–Al	10.3578	−112.8183	9.4511	−1.2318	−1.0544	0.1604
Al–O	11.0284	−28.5714	95.3424	−217.4885	242.7988	−107.0122
O–O	9.9306	−17.4669	25.3341	−19.0023	6.6210	−0.8289

Table 2. Potential function parameters.

	A (eV)	ρ (Å)	C (Å^6 eV)	r_0 (Å)	r_1 (Å)
Mg–Mg	—	—	—	0.5	1.05
Mg–Al	—	—	—	0.5	1.05
Mg–O	1279.69	0.299 69	—	0.15	0.8
Al–Al	—	—	—	0.3	1.05
Al–O	1374.79	0.301 3	—	0.15	0.8
O–O	9547.96	0.219 16	32.0	0.2	1.05

by gradually increasing this kinetic energy until permanently displaced atoms appear in the structure. Permanently displaced atoms are those that do not occupy their original lattice sites. They can either sit on other crystallographic sites or appear as interstitials. We define the vacancy radius v_R for the purposes of these calculations to be 0.84 Å, i.e. a site in the initial lattice becomes a vacancy during the dynamics if no atom lies within v_R of it. A similar definition applies to interstitials. The lattice atoms were brought to a certain temperature by adding kinetic energy and a displacement to each atom, followed by relaxation and equilibration before the PKA events were executed. To determine the energy displacement threshold, E_d, the heating temperature was chosen so that after the excess kinetic energy imparted by the PKA was dissipated the final temperature of the lattice was either 125 or 300 K. The final temperature resulted from an initially heated lattice followed by equilibration after the PKA event. This meant that the final temperature stabilized more quickly than if the edge atoms had been connected to a heat bath, which is a more common approach but requires more computing time for equilibration. As a result, it was found that trajectories used to determine E_d could be terminated after 2 ps. Higher energy trajectories were run for up to 10 ps with a system size containing up to 154 883 atoms (14-unit-cell cube). For low energy cascades, the smallest crystal size contained 3693 atoms (four unit cells).

3. Displacement energy thresholds

The PKA directions chosen are shown in table 3. For each PKA direction chosen, E_d was calculated from a single set of simulations for $T = 125$ K. However, three sets were used at 300 K because of the slightly larger displacements of the initial atom positions due to the thermal motion. It was found that E_d could vary depending on the precise layout of these initial positions. The resulting E_d given in table 3 for $T = 300$ K is therefore an average value. The cascade is initiated by the PKA which induces collisional sequences along the specified trajectory. The cascade damage typically reaches its peak after 60–80 fs, with a maximum of around 20 displaced atoms. For low threshold energies, only a few atoms are involved in the cascade. The system then relaxes, resulting in the annihilation of most of the defects and, if the

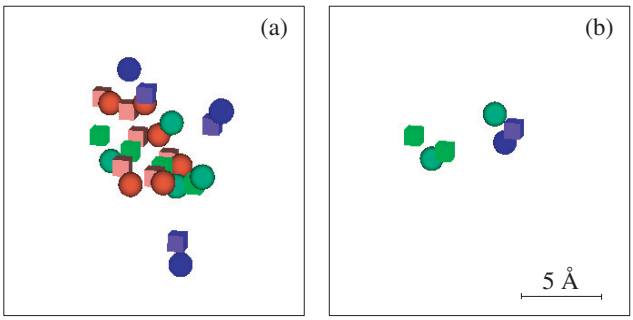

Figure 2. The damage in the lattice for an Al PKA projected in the ⟨053⟩ direction with 112.5 eV at 300 K. (a) The peak damage at $t = 80.9$ fs—interstitial atoms are plotted as spheres and vacancies as cubes. The red/medium grey colour indicates O defects, Al defects are in green/light grey and Mg in blue/dark grey. (b) The stable defects remaining at $t = 2$ ps. In this and subsequent figures the outlines are not representative of the size of the simulation box.

Table 3. Threshold displacement energies in eV.

PKA orientation	125 K			300 K (mean of 3 trajectories)		
	Mg PKA	Al PKA	O PKA	Mg PKA	Al PKA	O PKA
⟨232⟩	182.5	82.5	47.5	184.2	79.2	49.2
⟨111⟩	167.5	77.5	47.5	172.5	74.2	49.2
⟨211⟩	122.5	77.5	62.5	132.5	82.5	64.2
⟨100⟩	92.5	72.5	27.5	94.2	82.5	27.5
⟨141⟩	232.5	82.5	52.5	142.5	79.5	54.2
⟨318⟩	192.5	87.5	67.5	94.2	87.5	72.5
⟨836⟩	72.5	82.5	57.5	80.8	82.5	60.8
⟨053⟩	37.5	157.5	77.5	34.2	147.5	70.8
⟨712⟩	117.5	57.5	72.5	122.5	55.8	67.5
⟨793⟩	67.5	87.5	57.5	62.5	90.8	60.8
⟨110⟩	42.5	117.5	112.5	42.5	112.5	105.8
⟨151⟩	232.5	82.5	52.5	145.8	79.2	54.2
⟨131⟩	277.5	82.5	47.5	159.2	82.5	54.2

energy imparted to the PKA is large enough, a few permanent defects remain in the simulation box. Figure 2(a) shows the maximum lattice damage, which occurs after 81 fs, for an Al PKA in the ⟨110⟩ direction at the threshold energy of 112.5 eV, while the residual defects at the end of the simulation are illustrated in figure 2(b). The latter is composed of a split $Mg_i^{\cdot\cdot}$–V''_{Mg}–$Al_i^{\cdot\cdot\cdot}$ interstitial, in the simplified Kröger–Vink notation [13], where one Al and one Mg interstitial share the same Mg vacancy. The other remaining defect is an V'''_{Al}–$Al_i^{\cdot\cdot\cdot}$–V'''_{Al} split vacancy configuration where one Al interstitial is trapped between two Al vacancies.

E_d is found to be dependent on the PKA type, on the orientation of the PKA and on the temperature of the system. Along certain trajectories, where the PKA initially undergoes a direct (head-on) collision with a nearby atom, more energy is required to force the target atom away from its perfect lattice position. In other cases, the PKA is able to move easily along other 'open' paths between its first neighbours, requiring a lower E_d. A summary of the defects created for the 13 runs at 125 K is given in table 4 while the 39 runs performed at 300 K are summarized in table 5. The results shown in table 3 reveal that in general the O PKA has the lowest E_d, followed by Al and then Mg. In addition there were some large differences in E_d

Table 4. Distribution of defects at threshold energies calculated at 125 K for a total of 13 runs for each PKA.

PKA type	Ion swapping on same sublattice Mg/O/Al	Split interstitials: $Mg_i^{\cdot\cdot}$–V''_{Mg}–$Mg_i^{\cdot\cdot}$ pure Mg	Split interstitials: O_i''–$V_O^{\cdot\cdot}$–O_i'' pure O	Split interstitials: $Mg_i^{\cdot\cdot}$–V''_{Mg}–$Al_i^{\cdot\cdot\cdot}$ mixed Mg–Al	Anti-sites Al/Mg	N_{TFP} [a]	Perfect lattice
Mg	10/0/3	5	0	1	4/4	6	3
Al	2/0/14	0	2	2	4/4	4	5
O	0/13/0	0	9	0	0/0	9	4

[a] Total number of Frenkel pairs (vacancies).

Table 5. Distribution of defects at threshold energies calculated at 300 K for a total of 39 runs for each PKA.

PKA type	Ion swapping on same sublattice Mg/O/Al	Split interstitials: $Mg_i^{\cdot\cdot}$–V''_{Mg}–$Mg_i^{\cdot\cdot}$ pure Mg	Split interstitials: O_i''–$V_O^{\cdot\cdot}$–O_i'' pure O	Split interstitials: $Mg_i^{\cdot\cdot}$–V''_{Mg}–$Al_i^{\cdot\cdot\cdot}$ mixed Mg–Al	Anti-sites Al/Mg	N_{TFP}	Perfect lattice
Mg	29/37/1	2	4	6	10/15	9	19
Al	5/1/40	1	5	5	19/18	11	10
O	0/38/0	0	24	0	0/0	24	15

dependent on the exact initial positions of the lattice ions, for a fixed temperature. For example at 300 K the value of E_d for the Al PKA in the ⟨100⟩ direction varied by 72 eV from the lowest value of 50 eV to the highest at 122.5 eV. Averaged over all trajectories and PKA ions, the standard deviation in the value of E_d at 300 K was 12 eV but this value is larger for the case of head-on collisions. Another example of this can be seen when comparing the threshold values for the Al PKA in the ⟨053⟩ and ⟨110⟩ directions which in a perfect lattice should be identical. Part of this difference is due to phonon vibration. However, another reason is the way in which the positions of atoms in the initial lattice are computed. This is done by a process of relaxation from the initially perfect spinel structure with a varying u parameter. As a result the nearest neighbours from an Al ion are not precisely located in the ⟨053⟩ and ⟨110⟩ directions but relax slightly differently and differ from these directions very slightly, in fact by less than 0.5°. This small difference from a head-on collision combined with phonon effects produces a much larger variation in the displacement energy thresholds, a good illustration of the chaotic nature of collision cascades where small changes in initial conditions can give large changes in individual trajectories.

Near head-on collisions with close inter-ionic separation also correspond to high displacement energy thresholds. For example, at 125 K the highest value of E_d occurred for the Mg undergoing a direct collision with an Al ion along ⟨131⟩.

3.1. Mg PKA

In order to gain more physical insight into the numbers presented in tables 3–5, we examine trajectories with high and low values of E_d in more detail. In particular, we examine the Mg PKA in the ⟨111⟩ direction, which was directed towards its O neighbour; that along ⟨131⟩, which targeted an Al ion, and those along ⟨053⟩, ⟨232⟩ and ⟨151⟩.

Table 3 shows that the highest E_d recorded for $T = 125$ K was along the ⟨131⟩ direction with a value of 277.5 eV. During this collision cascade the Mg PKA underwent a head-on

collision with a neighbouring Al ion, creating a maximum of 18 displaced ions at a time of 90 fs and resulting in two Mg ions swapping sites. However, no permanent defects were created in the lattice.

The smallest value for E_d was 34.2 eV, occurring along the ⟨053⟩ direction at 300 K. During this process, the Mg PKA interacted with a nearest Mg neighbour and temporarily shared the same site. Only the two Mg ions were displaced: the two interstitials rotated about the single Mg vacancy until one interstitial was attracted to the nearby vacant site left by the PKA. This resulted in both ions swapping positions, leaving the crystal structure unchanged.

A relatively high energy was required to displace atoms along the ⟨111⟩ direction. For this direction the PKA first collided with an O ion, momentarily occupying this O site. Due to the repulsive Coulombic forces, the Mg ion was ejected from the site and a maximum of 26 displaced ions were formed at time $t = 60$ fs. All the defects annealed by 360 fs, leaving a perfect lattice where only two O ions had swapped positions. Another high value of E_d was 182.5 eV along the ⟨232⟩ direction in which the PKA underwent a near direct collision with a neighbouring oxygen ion. This resulted in stable defects consisting of one isolated O vacancy and two O interstitials sharing a common vacant site as a split interstitial (O_i''–$V_O^{\cdot\cdot}$–O_i'') along $\langle 1\bar{1}0\rangle$.

A high value of E_d was also recorded along ⟨151⟩ which represents another near direct collision with an O ion. It is noted that these high energy thresholds at the lower temperature are reduced considerably at 300 K. Related directly to this reduction in E_d is a large increase in the number of O ions that exchange sites, from zero to 37, as the temperature increases. This increase comes almost entirely from the high index directions that have high E_d values, due to the larger deflections that can occur as a result of increased lattice vibration which means that the PKA's first impact is no longer a direct head-on collision. These directions are also those with the largest variance in E_d at 300 K.

3.2. Al PKA

The smallest E_d for an Al PKA was 55.8 eV at 300 K, along the ⟨712⟩ direction. Along this path, the PKA instantly displaced one of its closest O neighbours and a nearby Mg. The cations quickly reverted to their initial lattice sites while the O interstitial combined with another O ion to form a stable split interstitial in the ⟨101⟩ direction. At 125 K, the highest energy required to permanently displace an atom was 157.5 eV along the ⟨053⟩ direction. In this case, the Al PKA was directed towards another Al ion. This cascade involved replacement sequences of one Al and two Mg ions over their respective sublattices. The system stabilized after 330 fs with the formation of one Al and one Mg antisite defect. One point to observe with both the Al and Mg PKA is the relatively small number of the other cation species that exchange sites compared to the number of antisite defects. This appears to be due entirely to the larger number of displaced ions on the PKA species sublattice.

3.3. O PKA

For the O PKAs, all of the permanently displaced ions were always oxygen, and, in each case in which there was residual damage, the only defects left after the cascade were a single O split interstitial and an isolated O vacancy. The lowest E_d was 27.5 eV at 125 K, along the ⟨100⟩ direction. The oxygen PKA was deflected by its first Mg neighbour and then collided with another O ion. This interaction finally led both of these oxygen ions to form an O_i''–$V_O^{\cdot\cdot}$–O_i'' split interstitial defect. The highest E_d was recorded along the ⟨110⟩ direction and was 112.5 eV at 125 K. Along this direction the PKA collided directly with another oxygen ion. Initially

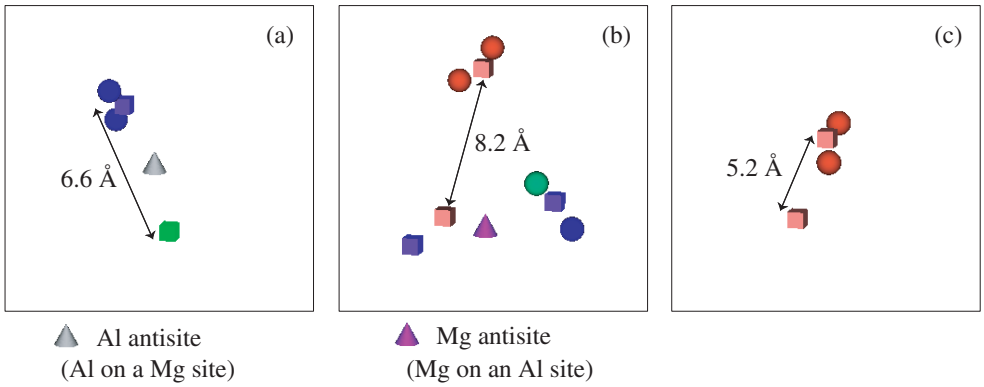

Figure 3. Some final defects seen at threshold energies. (a) one $Mg_i^{\cdot\cdot}$–V''_{Mg}–$Mg_i^{\cdot\cdot}$ split interstitial, one Al antisite and one Al vacancy for an Al PKA at 300 K ($E_d = 122.5$ eV); (b) one O_i''–$V_O^{\cdot\cdot}$–O_i'' and one $Mg_i^{\cdot\cdot}$–V''_{Mg}–$Al_i^{\cdot\cdot\cdot}$, one O and one Mg vacancy and one Mg antisite for an Mg PKA at 300 K; (c) one O_i''–$V_O^{\cdot\cdot}$–O_i'' and one isolated O vacancy for an O PKA at 125 K ($E_d = 47.5$ eV).

there were six displaced ions—three O, two Mg and one Al—but the cations returned to their original sites within 120 fs. The remaining defects consisted of an O split interstitial and an isolated O vacancy. The O defects annealed through a series of replacement sequences of interstitials over the O sublattice, towards the isolated vacancy, yielding a perfect lattice with exchanged O ions.

Williford *et al* [14] derived the threshold displacement energies for various ceramic materials using the GULP code. The authors reported E_d values for $MgAl_2O_4$ ranging from 22 to 76 eV on the O sublattice depending on the direction, and values of 60 and 51 eV for Mg and Al ions respectively. However, in that study, only a small number of trajectories were calculated. In this present work, a larger spectrum for E_d is observed due to a wider range of initial directions chosen for the PKA.

3.4. Defect analysis

For PKA energies near E_d, the only defects formed were split interstitials or cation antisite defects. The split interstitial structures at the threshold energy regimes consist of either two oxygen ions sharing an oxygen lattice site, two Mg ions sharing an Mg site or split Mg–Al interstitials sharing a vacant Mg site. Tables 4 and 5 summarize the total number of defects and figure 3 illustrates the arrangement of typical residual defects obtained at the displacement thresholds. Because the most common defects observed in the cascades were split interstitials, and we will later compare defect numbers with those in MgO (where the isolated interstitials exist at the unit cell centre and are not split), a split interstitial separated from an isolated vacancy is counted as a single Frenkel pair only.

Antisite defects were only observed when the PKA was a cation. The energy associated with the formation of antisite pairs was calculated as a function of separation. That is, one Mg ion swapped with one Al ion and the energy of this system was minimized. This was done for various separations of the swapped ions and the results are given in figure 4. The lowest formation energy was found to be 0.8 eV for the case when the pair of Mg and an Al antisite were nearby, only 3.35 Å apart. This energy became larger with increasing defect separation. Previous work by Pandey *et al* [15] on zinc aluminate and zinc gallate spinels predicted a formation energy of 1.7 eV for Zn and Al antisites in $ZnAl_2O_4$ and an energy of 0.9 eV for

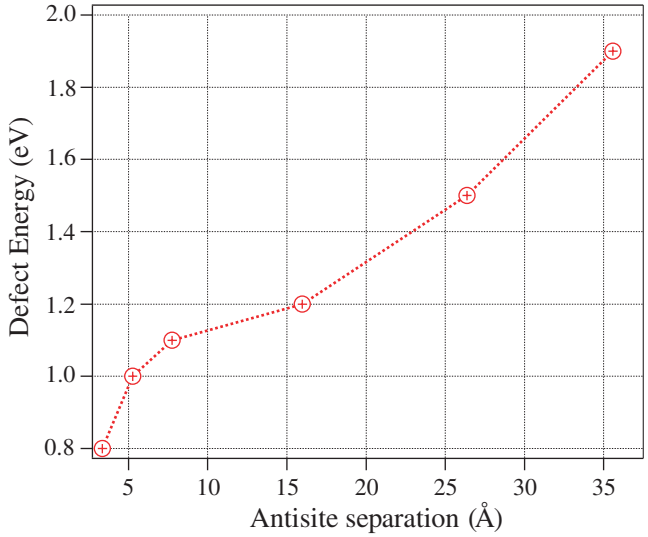

Figure 4. Defect energies for Mg–Al antisite pairs and their variation with antisite separation.

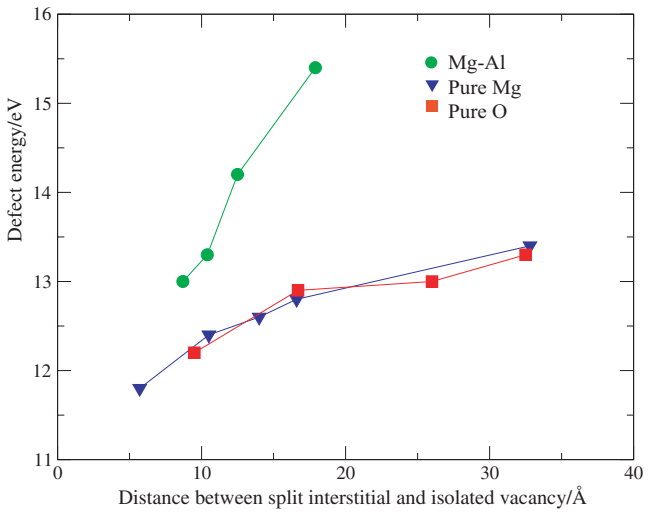

Figure 5. Defect energies for the different split interstitial defects as a function of distance between the defect centre and its corresponding isolated vacant site.

Zn and Ga antisites in $ZnGa_2O_4$. In the present work, antisites involving anion and cation exchanges were found to be unstable.

In the low energy cascades, pure Mg and O split interstitials and Mg–Al ions split around an Mg vacancy were formed but neither pure Al split interstitials nor Mg–Al ions around an Al vacancy occurred. The relative stability of the observed defects can be determined from their corresponding defect energies, which have been calculated using the same methodology as described above for the antisite defects. The results are illustrated in figure 5. It can be seen from figure 5 that the pure Mg and O defect energies are quite similar but the energy of the $Mg_i^{\cdot\cdot}$–V''_{Mg}–$Al_i^{\cdot\cdot\cdot}$ split interstitial is higher. Furthermore, as the separation between the

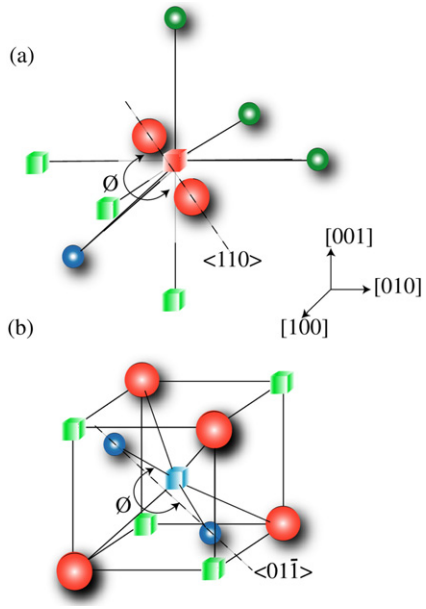

Figure 6. Environment of the defects in the crystal. (a) One of the possible configurations for O_i''–$V_O^{\cdot\cdot}$–O_i'', along ⟨110⟩ with $\phi = 137.6°$. (b) $Mg_i^{\cdot\cdot}$–V_{Mg}''–$Mg_i^{\cdot\cdot}$ along ⟨01$\bar{1}$⟩ where the interstitials are close to vacant octahedral sites.

interstitials and their vacant site increases, the energy of the defect also increases. The stability of the defects depends on their separation from the isolated vacancy, their orientation and the complex electric field between them. If the system has sufficient vibrational kinetic energy, the defects can anneal through the motion of interstitials back to the nearest vacancy. This is a common mechanism for the pure O split interstitials to anneal, and this recombination process occurs only on the O sublattice. In the case of cations, the same mechanism is observed for the annihilation of pure Mg split interstitials, but for the split $Mg_i^{\cdot\cdot}$–V_{Mg}''–$Al_i^{\cdot\cdot\cdot}$ interstitial the presence of cation vacancies can lead to the ultimate formation of antisite defects, the most stable defects in the system. Again, the migration of the cation interstitials during this annihilation process occurs on either of the cation sublattices. Vacancies are observed to be immobile during the collisional phase of the cascade.

It was found that the split interstitials were all orientated along the ⟨110⟩ directions. The defects are not linear and the interstitials subtend an angle with the site they share. Thus they are not pure dumbbell defects as, for example, in α-Fe where this angle is 180°. Figure 6 shows the O interstitials aligned along the ⟨110⟩ direction with an angle $\phi = 137.6°$ and Mg interstitals along ⟨01$\bar{1}$⟩ with $\phi = 124.8°$. In the case of $Mg_i^{\cdot\cdot}$–V_{Mg}''–$Mg_i^{\cdot\cdot}$ and $Mg_i^{\cdot\cdot}$–V_{Mg}''–$Al_i^{\cdot\cdot\cdot}$ the interstitials were close to octahedral interstices, but in the case of the O interstitial the interstitial atoms were relatively far from both the tetrahedral and octahedral sites. On average, the angle for $Mg_i^{\cdot\cdot}$–V_{Mg}''–$Al_i^{\cdot\cdot\cdot}$ is $\phi = 128.5°$ (averaged over nine defects), $\phi = 128.8°$ for the pure Mg defect (averaged over 20 structures) and $\phi = 130.9°$ for the pure O defect (averaged over 23 defects).

The results for the defect energies clearly show that antisite defects on cation sublattices are more likely to form than other defects such as split interstitials. Chen *et al* [16] also predicted antisite defects to be the most energetically favourable defects in $MgAl_2O_4$ because their arrangement involves the smallest distortion of the lattice compared to other defects.

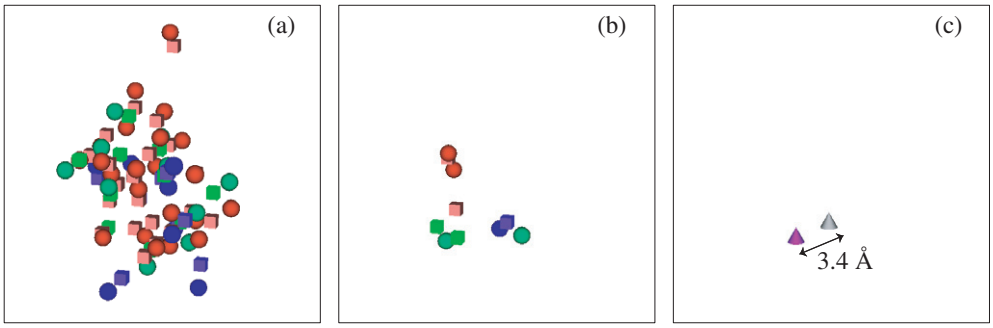

Figure 7. Collision cascade initiated by an Al PKA at 400 eV. (a) Peak damage at 123.4 fs; (b) metastable defects after 586.0 fs consisting of one Al split vacancy defect, one Mg–Al split interstitial, one O split interstitial and one O vacancy; (c) final defects at 1110.6 fs are one Mg and one Al antisite defect.

One other common defect observed was the V'''_{Al}–$Al^{\cdots}_{i}$–V'''_{Al} split vacancy defect (figure 2(b)), where an Al ion sits between two Al vacancies. Here the Al interstitial becomes trapped between the two Al vacancies at an initially unoccupied tetrahedral site.

4. Higher energy cascades

As discussed, PKAs at the threshold energy produce little to no residual damage. In irradiation environments, materials often undergo collisions of much higher energies. In order to obtain a better understanding of how spinel behaves in more violent conditions, simulations of higher energy PKAs were performed. Nine runs for each of the Mg, Al and O PKAs were done at 400 eV and four runs for each PKA species were performed at PKA energies of 2 and 5 keV, comprising a total of 12 simulations for each of these higher energies.

4.1. 400 eV cascades

A typical cascade resulting from a 400 eV Al PKA, initiated in the ⟨789⟩ direction, is illustrated in figure 7. The energetic particle sets off, forcing other ions out of their perfect lattice sites. The number of displacements peaks at 123.4 fs with a total of 40 displaced ions, about half of which are oxygen ions (figure 7(a)). After 586.0 fs most of the defects have annealed, leaving behind four defects: $Mg^{\cdot\cdot}_{i}$–V''_{Mg}–$Al^{\cdots}_{i}$, V'''_{Al}–$Al^{\cdots}_{i}$–V'''_{Al}, O''_{i}–$V^{\cdot\cdot}_{O}$–O''_{i} and an isolated O vacancy (figure 7(b)). The O defects recombined through replacement mechanisms over the O sublattice while the V'''_{Al}–$Al^{\cdots}_{i}$–V'''_{Al} was reduced to only an Al vacancy, which then attracted the Mg cation in the Mg–Al split interstitial. After 1110.6 fs, the system reached a stable configuration with the formation of two antisite defects (figure 7(c)).

For the O PKA, of the nine simulations performed, three resulted in a perfect lattice configuration. During these simulations, two O split interstitials remained after the collisional phase with the corresponding number of isolated vacancies. The perfect crystal structure was recovered through a series of replacement mechanisms over the O sublattice as shown in figure 8. Most of the other cascades resulted in the formation of an O split interstitial defect with an isolated vacancy further separated than that which recombined in figure 8. In one case, in which the PKA was directed along the ⟨789⟩ direction, two cation antisite defects formed. A similar recombination mechanism was also observed for cascades in MgO [17, 18].

In addition to the defects obtained at the threshold energies, some cation–anion vacancy pairs were also observed at 400 eV. For cation PKAs, about twice as many Frenkel pairs were

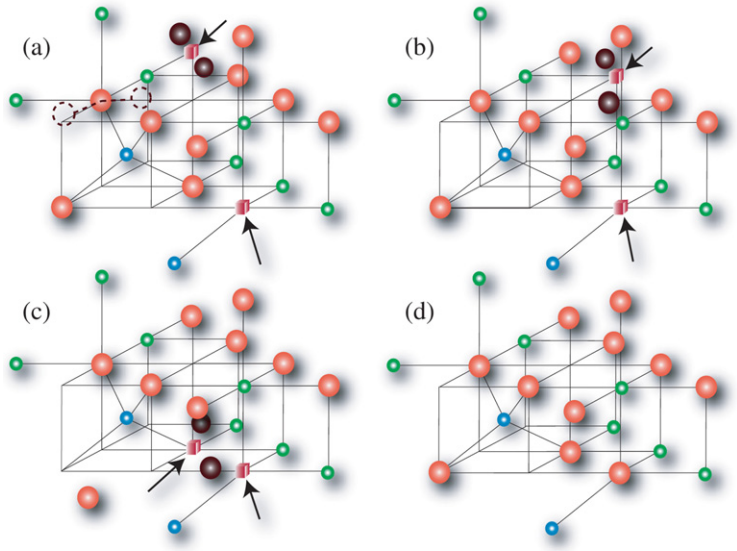

Figure 8. The migration of O split interstitial towards an O vacancy due to strong Coulomb attraction, yielding a perfect lattice structure. Initially defects were separated by 7.7 Å. (a) The initial interstitial formation which remained stable from 735 to 1485 fs after the start of the cascade; (b) 1511 fs; (c) 1536 fs; (d) 1560 fs. The dotted outline in (a) represents the position of the stable split interstitial with respect to the vacancy that formed in figure 3(c). The vacant sites are marked by the arrows. In this case the split interstitial would have to rotate and overcome a larger energy barrier to recombine with the vacancy.

Table 6. Table of residual defects for 400 eV cascades.

	Split interstitial defects							
PKA type	Pure Mg	Pure O	Mixed Mg–Al	Iso. vac. Mg/Al/O	Vac. pairs Mg–O/Al–O	Antisites Al/Mg	Al complex[a] vac. split	N_{TFP}
Mg	8	1	2	9/0/0	1/0	4/6	0	9
Al	5	4	1	0/3/1	0/1	10/5	2	7
O	0	5	0	0/0/5	0	1/1	0	5

[a] The Al complex consists of one Al split vacancy defect which also has an O vacancy next to one of its Al vacancies, as illustrated at C in figure 9(a). Nine simulations were performed for each PKA.

produced compared to O PKAs, as well as more antisite defects. The distribution of all the defects are given in table 6. In this and subsequent tables, the column labelled 'iso. vac.' refers to single vacancies that were separated from other vacancies but might lie close to other defects such as an antisite.

4.2. 2 keV cascades

As in MgO [17, 18], collision cascades at 2 keV resulted in the production of more defects in the crystal compared to 400 eV cascades. Typical defect distributions after a 2 keV PKA event are illustrated in figure 9 for Al PKAs along two different directions. PKAs travelled up to 50 Å before coming to rest, creating defects along their path. The various defect structures described previously were observed, but along certain trajectories clusters of defects were also formed. One such defect on the Al sublattice consisted of three Al ions which were displaced from perfect octahedral to interstitial tetrahedral sites between three Al vacancies

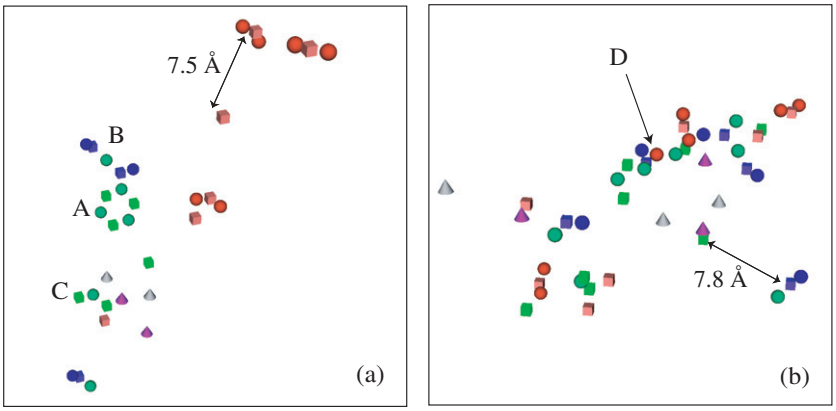

Figure 9. Residual defects generated at 2 keV for Al PKAs. (a) Well defined and separated defects were obtained for a PKA trajectory of ⟨210⟩; (b) for the projectile aimed along ⟨232⟩, the defects were much closer together. The labelled defects are A, Al 'ring' defect; B, extended Mg–Mg–Al crowdion; C, Al vacancy split with O vacancy; D, O interstitial lying between cation interstitials.

Table 7. Table of residual defects for 2 keV cascades.

PKA type	Split interstitial defects			Iso. vac. Mg/Al/O	Vac. pairs Mg–O/Al–O	Antisites Al/Mg	Al complex Ring[a] /vac. slit	N_{TFP}
	Pure Mg	Pure O	Mixed Mg–Al					
Mg	11	12	5	10/2/10	2/0	7/9	0	32
Al	2	10	11	0/8/5	0	11/9	2/5	37
O	0	14	5	0/1/10	0/3	3/3	0/3	34

[a] The Al 'ring' defect is the structure illustrated at A in figure 9(a), $Al_i^{\cdot\cdot\cdot}$–$V_{Al}^{\cdot\cdot\cdot}$–$Al_i^{\cdot\cdot\cdot}$–$V_{Al}^{\cdot\cdot\cdot}$–$Al_i^{\cdot\cdot\cdot}$–$V_{Al}^{\cdot\cdot\cdot}$, in the Kröger–Vink notation.

in a vacancy–interstitial 'ring' configuration, labelled A in figure 9(a). A second extended defect produced on the cation sublattice comprised a crowdion, i.e. an Mg–Al split interstitial with an extra Mg vacancy and Mg interstitial, marked B in figure 9(a). A similar type of crowdion defect, composed of three interstitials sharing two lattice sites, was seen on the O sublattice. Clustering occurred only for PKAs in certain directions; along other directions only well defined and distinct defects, such as split interstitials, antisites, Al split vacancy defects, and isolated vacancies, were formed. Table 7 lists the total number of defects for each of the four runs for the three different PKA ions. For the Mg PKA directed along ⟨210⟩, one larger cluster was observed, composed of three O ions sharing one site and an Al antisite, together with separated vacancies formed earlier along the ion path. Isolated interstitials were rare: out of all of the trajectories, only two were observed: one Mg and one O interstitial.

4.3. 5 keV cascades

At a PKA energy of 5 keV, some cascades subdivided into distinct subcascades and spread over a larger volume of the computational box. This resulted in the production of a larger variety of defects, including vacancy clusters and cation and anion interstitial–vacancy chains, in addition to the types of defects described previously. Table 8 shows the main defects obtained for the four runs carried out for each PKA type. At such energy regimes it was found that 58% of the split interstitial defects were pure O. Also, the O PKAs were able to create a larger number of antisite defects compared to lower energy cascades.

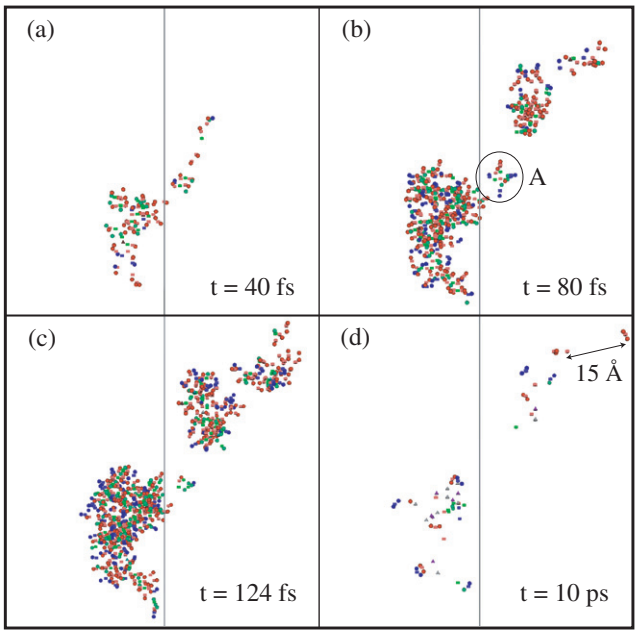

Figure 10. The formation and recombination of interstitials, vacancies and antisite defects during the cascade for a 5 keV Mg PKA in the ⟨113⟩ direction. The vertical line in the image defines the direction of one of the crystal axes. The small subcascade labelled A has peak damage at 80 fs but at the end of the simulation disappears completely.

Table 8. Table of main residual defects for 5 keV cascades.

PKA	Split interstitial defects			Iso. vac.	Vac. pairs	Antisites	Al complex	
type	Pure Mg	Pure O	Mixed Mg–Al	Mg/Al/O	Mg–O/Al–O	Al/Mg	Ring/vac.-split	N_{TFP}
Mg	15	25	9	3/8/10	1/0	31/24	3/6	69
Al	10	36	8	0/6/16	2/6	28/17	1/6	66
O	13	27	8	1/5/14	1/4	36/29	1/12	86

The development of a typical collision cascade is shown in figure 10. Here an Mg ion was projected in the ⟨113⟩ direction. Even at 5 keV distinct subcascades are recognizable. In figure 10(b) four such sub-cascades can be distinguished and one such sub-region, labelled A, completely reanneals by the end of the simulation. This figure shows a larger number of antisite defects in the densest sub-cascade region near to where the PKA originated.

The damage remaining after three different cascades at 5 keV are illustrated in figure 11. It was found that even after the collisional phase (after 10 ps), some defects remained in a state of oscillation between adjacent states separated by small energy barriers. For example, in a few cases, an extended $Mg_i^{\cdot\cdot}$–V''_{Mg}–$Al_i^{\cdot\cdot\cdot}$–V''_{Mg}–$Mg_i^{\cdot\cdot}$ crowdion, sharing two vacant sites, could oscillate between this structure and the normal Mg–Al split configuration. This was also observed for the extended O crowdions. On the other hand, the Al ring structures were very stable. The formation energy of this defect was found to be 9.4 eV. Another defect observed, labelled A in figure 11(a), was that of a vacancy cluster comprising four Al, two O and one Mg vacancies with two Al interstitials, one of which lies between an Mg and an Al vacancy. Also observed was a cluster composed of an O split interstitial linked with an extra O interstitial next to a Mg–Al split interstitial, labelled F in figure 11(c).

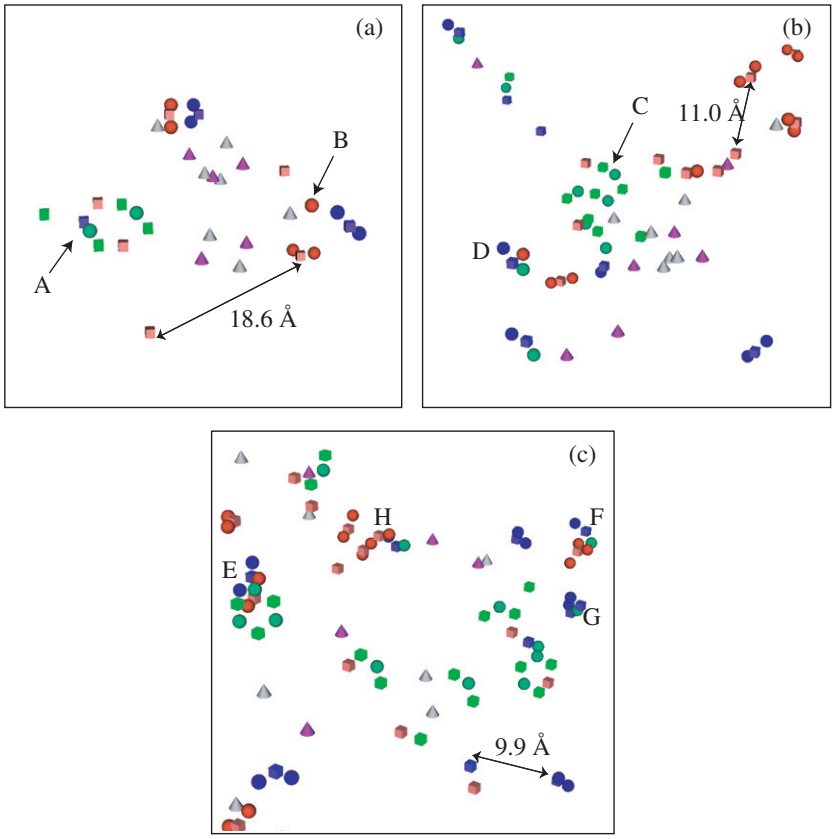

Figure 11. A picture showing many features of the residual damage after the collisional phase of the cascade, 10 ps, at a PKA energy of 5 keV. (a) For an Mg PKA with trajectory ⟨113⟩, a core rich in antisite defects is obtained. Part of the defect labelled A contains an Al interstitial trapped between Al and Mg vacancies; defect B represents an O interstitial which lies close to an Al antisite. (b) Along ⟨134⟩ the Mg PKA yields other defects: C indicates an incomplete Al 'ring' structure due to the presence of a nearby O vacancy, and D shows a cluster made up of an Mg–Al split interstitial with an extra O interstitial. (c) Defects created for an O PKA along ⟨323⟩ which are more clustered: E denotes a cluster consisting of an Al ring with one O and Mg split interstitials. Cluster F consists of an Mg–Al split interstitial with an O split interstitial and an extra O interstitial. H and G represent extended crowdions over the anion and cation sublattice respectively.

5. Comparison with MgO

These results can be compared with similar calculations performed on MgO [17, 18]. Radiation damage in MgO for the same PKA energies is characterized by similar high defect formation energies, but with a smaller variety of defects, a relatively small amount of defect clustering, isolated interstitials and Mg–O di-interstitial defects which diffuse on the timescale of nanoseconds and 0.1 s, respectively, at room temperature. Such di-interstitial defects have not been observed to form in spinel and most point defect interstitials were of the split form. In fact, no stoichiometric or sub-stoichiometric (such as MgO or Al_2O_3) defects were produced in any of the cascades. The strong Coulomb fields in MgO result in isolated interstitials very quickly recombining with nearby vacancies. The vacancy–interstitial recombination mechanism due to strong Coulomb attraction was also observed in spinel over picosecond timescales, as shown in figure 8.

Ignoring the antisite defects, the average number of residual Frenkel pairs that remain after the collisional phase of the cascade is slightly more for spinel than for MgO at 400 eV at an average of 0.8 FPs per trajectory for spinel compared to 0.65 per trajectory for MgO. At 2 keV there are approximately 8.6 FPs per trajectory for spinel compared to 7 per trajectory for MgO whereas at 5 keV the numbers are 18.4 and 18.0 respectively. This suggests that the defect damage in both materials during the collisional phase of the cascade is very similar with possibly more damage in MgO as the PKA energy increases. Higher energy cascades in both materials are currently under investigation. However, in the PKA energy range up to 5 keV, most defects in MgO would reanneal quickly since isolated interstitials and di-interstitials are mobile at room temperature and would quickly recombine with the immobile vacancies [17, 18]. Preliminary investigations in spinel indicate that relatively low energy barriers for diffusion would also imply that interstitial defects would be mobile at room temperature.

Another observation obtained from the examination of individual cascades in MgO is that di-vacancies are common defects observed in 5 keV cascades in MgO. In addition radiation damage in MgO has some characteristics of metals whereby vacancies tend to form in the core of the cascade and along the PKA path with interstitials on the periphery. This is not the case in spinel, where, as can be seen from the typical example shown in figure 10, the core of the cascade has more antisite defects than vacancies. This suggests that antisite (as opposed to vacancy) formation is one of the key factors for the relative radiation resistance of spinel compared to MgO.

6. Conclusion

Point defect formation in spinel was studied both at near-threshold energies and at higher energies of 400 eV, 2 and 5 keV. The threshold energies were derived for each of Mg, Al and O PKAs. The smallest E_d obtained was for an O PKA with a value of 27.5 eV while the largest energy recorded was 277.5 eV for an Mg PKA. In all of the energy regimes studied in this work, split interstitials and cation antisites were the predominant defect configurations formed. The split interstitials were aligned with their axes along $\langle 110 \rangle$. Higher energy cascades generated more Frenkel pairs and a wider variety of defects. It was also found that Al ions could occupy empty tetrahedral sites in the lattice by forming split vacancy and ring defects. Other observations include the following.

(i) For the 300 K threshold displacement runs the Al PKAs generate more damage than the others, at least from the point of view that fewer crystals return to their perfect lattice.
(ii) O PKAs generate relatively few anti-site defects at low energy, but at high energy they seem to be the dominant generator of antisites. They are also the easiest PKAs to generate.
(iii) The number of isolated Mg vacancies goes down with energy, while the other types seem to go up. This implies that Mg vacancies are more likely to form complexes as the energy increases.

As would be expected, the high values for E_d and the strong Coulomb attraction between defects mean that spinel is a material that is resistant to radiation. The damage induced by collision cascades in spinel as measured by the number of Frenkel pairs produced is very similar to MgO. This damage is not sufficient to distinguish between the relative radiation tolerance of the two materials since damage recovery and the effect of dose needs to be also considered. For example, the ring defect which is formed in spinel but which has no counterpart in MgO is classified as three Frenkel pairs. However, the displaced atoms can revert to a perfect lattice by one concerted motion with a relatively low energy barrier. Thus, as well as the amount of damage created after the collisional phase of a cascade, it is also necessary to

determine diffusion barriers in order to assess the long timescale effects. Diffusion barriers for typical defects formed in spinel have not yet been calculated and these will form the basis of a more extended study that will allow the radiation tolerance of spinel to be more fully and quantitatively understood and described.

Acknowledgments

This work was supported by the United States Department of Energy, Office of Science, Office of Basic Energy Sciences, Division of Materials Sciences and Engineering and a Loughborough University PhD studentship.

References

[1] Park B, Weber W J and Corrales L R 2001 *Phys. Rev.* B **64** 174108
[2] Chartier A, Meis C, Crocombette J, Corrales L R and Weber W J 2003 *Phys. Rev.* B **67** 174102
[3] Devanathan R, Yu N, Sickafus K E and Nastasi M 1996 *J. Nucl. Mater.* **232** 59
[4] Sickafus K E, Minervini L, Grimes R W, Valdez J A, Ishimaru M, Li F, McClellan K J and Hartmann T 2000 *Science* **289** 748
[5] Kashii N, Maekawa H and Hinatsu Y 1999 *J. Am. Ceram. Soc.* **82** 1844
[6] Sickafus K E, Wills J M and Grimes N W 1999 *J. Am. Ceram. Soc.* **82** 3279
[7] Catlow C R A, Diller K M and Norgett M J 1977 *J. Phys. C: Solid State Phys.* **10** 1394
[8] Ziegler J F, Biersack J P and Littmark U 1985 *The Stopping and Range of Ions in Solids* vol 1 (Oxford: Pergamon)
[9] Greengard L and Rokhlin V 1985 *J. Comput. Phys.* **60** 187
[10] Trachenko K, Dove M T and Salje E K H 2003 *J. Phys.: Condens. Matter* **15** L1
[11] Cynn H, Sharma S K, Cooney T F and Nicol M 1992 *Phys. Rev.* B **45** 500
[12] Sheldon R I, Hartmann T, Sickafus K E, Ibarra A, Scott B L, Argyiou D N, Larson A C and Von Dreele R B 1999 *J. Am. Ceram. Soc.* **82** 3293
[13] Kröger F A and Vink H A 1957 *Solid State Physics: Advances in Research and Applications* (New York: Academic)
[14] Williford R E, Devanathan R and Weber W J 1998 *Nucl. Instrum. Methods* B **141** 94
[15] Pandey R, Gale J D, Sampath S K and Recio J M 1999 *J. Am. Ceram. Soc.* **82** 3337
[16] Chen S P, Yan M, Gale J D, Grimes R W, Devanathan R, Sickafus K E, Yu N and Nastasi M 1996 *Phys. Mag. Lett.* **73** 51
[17] Uberuaga B P, Smith R, Cleave A R, Grimes R W, Montalenti F, Henkelman G, Voter A F and Sickafus K E 2004 *Phys. Rev. Lett.* **92** 115505
[18] Uberuaga B P, Smith R, Cleave A R, Grimes R W, Henkelman G, Voter A F and Sickafus K E 2004 *Phys. Rev.* B at press